



**HAL**  
open science

## Highly sensitive H<sub>2</sub>O<sub>2</sub> sensor based on porous bimetallic oxide Ce<sub>1-x</sub>Tb<sub>x</sub>O<sub>y</sub> derived from homeotypic Ln-MOFs

Lei Zhao, Kaian Sun, Nuerguli Youliwasi, Hailing Guo, Ge Yang, Feng Jiao, Bin Dong, Yongming Chai, Svetlana Mintova, Chenguang Liu

### ► To cite this version:

Lei Zhao, Kaian Sun, Nuerguli Youliwasi, Hailing Guo, Ge Yang, et al.. Highly sensitive H<sub>2</sub>O<sub>2</sub> sensor based on porous bimetallic oxide Ce<sub>1-x</sub>Tb<sub>x</sub>O<sub>y</sub> derived from homeotypic Ln-MOFs. Applied Surface Science, 2019, 470, pp.91-98. 10.1016/j.apsusc.2018.10.278 . hal-01992005

**HAL Id: hal-01992005**

**<https://normandie-univ.hal.science/hal-01992005>**

Submitted on 27 Nov 2020

**HAL** is a multi-disciplinary open access archive for the deposit and dissemination of scientific research documents, whether they are published or not. The documents may come from teaching and research institutions in France or abroad, or from public or private research centers.

L'archive ouverte pluridisciplinaire **HAL**, est destinée au dépôt et à la diffusion de documents scientifiques de niveau recherche, publiés ou non, émanant des établissements d'enseignement et de recherche français ou étrangers, des laboratoires publics ou privés.

# Highly Sensitive H<sub>2</sub>O<sub>2</sub> Sensor Based on Porous Bimetallic Oxide Ce<sub>1-x</sub>Tb<sub>x</sub>O<sub>y</sub>

## Derived from Homeotypic Ln-MOFs

Lei Zhao<sup>a, Δ</sup>, Kaian Sun<sup>a, Δ</sup>, Nuerguli Youliwasi<sup>a</sup>, Hailing Guo<sup>a, \*</sup>, Ge Yang<sup>a</sup>, Feng Jiao<sup>a</sup>, Bin Dong<sup>a</sup>, Yongming Chai<sup>a</sup>, Svetlana Mintova<sup>a, b</sup>, Chenguang Liu<sup>a</sup>

a: State Key Laboratory of Heavy Oil Processing, Key Laboratory of Catalysis, China National Petroleum Corp. (CNPC) China University of Petroleum (East China), Qingdao 266555, P. R. China E-mail: guohl@upc.edu.cn; Fax: +86 532 86981787; Tel: +86 532 86981716

b: Laboratoire Catalyse et Spectrochimie (LCS), CNRS, ENSICAEN, Université de Caen, 6 boulevard du Maréchal Juin, 14050 Caen France.

Δ: This author contributed equally to this work

[\*] Dr. Hailing Guo

**Abstract:**

Development of a sensitive and reliable method towards detection of hydrogen peroxide ( $\text{H}_2\text{O}_2$ ) is important for biomedical and environmental applications. The preparation of electrochemical sensors with high selectivity and sensitivity toward  $\text{H}_2\text{O}_2$  using porous homeotypic bi-metallic  $\text{Ce}_{1-x}\text{Tb}_x\text{O}_y$  crystals is reported. The porous homeotypic bi-metallic  $\text{Ce}_{1-x}\text{Tb}_x\text{O}_y$  crystals are prepared by direct pyrolysis of  $\text{Ce}_x\text{Tb}_{1-x}$ -MOFs precursors. The porous homeotypic bi-metallic  $\text{Ce}_{1-x}\text{Tb}_x\text{O}_y$  crystals are deposited on glassy carbon electrodes, and subsequently apply for detection of  $\text{H}_2\text{O}_2$  in an alkaline media. The porous  $\text{Ce}_{1-x}\text{Tb}_x\text{O}_y$  layers show high stability, high sensitivity toward  $\text{H}_2\text{O}_2$  ( $1.6831 \mu\text{A}\cdot\text{Mm}^{-1}$ ) ( $12.99 \mu\text{A}\cdot\text{mM}^{-1}\cdot\text{cm}^{-2}$ ) in a broad linear range ( $0.1 \mu\text{M}$  -  $4.2 \text{ mM}$ ) with a detection limit of  $7.7 \mu\text{M}$  ( $\text{S/N} = 3$ ), and fast response (less than 10 s).

**Keywords:** Sensor; Hydrogen peroxide; Porous homeotypic bi-metallic  $\text{Ce}_{1-x}\text{Tb}_x\text{O}_y$ ; MOFs; Density function theory

## 1. Introduction

Hydrogen peroxide ( $\text{H}_2\text{O}_2$ ), as a by-product of aerobic metabolism of enzymatic reactions, is widely applied in semiconductor, plastic, and food industry. It is well known that the  $\text{H}_2\text{O}_2$  is low-toxic but easily damage lipids, proteins and carbohydrates. It can even cause cancer on account of its oxidizing capability when accumulating to a certain amount in human body [1]. Therefore, the development of a sensitive and reliable method to determine the  $\text{H}_2\text{O}_2$  is important for biomedical and environmental applications.

Up to now, many techniques have been used to detect  $\text{H}_2\text{O}_2$ , including spectrophotometry [2,3], chemiluminescence [4-7], fluorometry [8-11], titrimetric, and electrochemistry [12-16]. Especially, the electrochemical approach with high sensitivity and easy handling, is receiving more attention during the last decades. It is well known that electroactivity mainly depends on electrode modified materials. Enzyme as a common electrode modified material, is fast, sensitive and simple for  $\text{H}_2\text{O}_2$  detection, but its stability is strongly affected by variation of the pH, temperature and concentration of analyte. Therefore, significant attention is focused on the fabrication of stable nonenzymatic sensor for  $\text{H}_2\text{O}_2$ . Precious metals (*e.g.* gold, silver, platinum, and rhodium) as active electrode modifier materials show great stability and sensitivity in the detection of  $\text{H}_2\text{O}_2$  [17-19]. However, the high price limited their application. Recently, metal oxides (*e.g.*  $\text{Co}_3\text{O}_4$ ,  $\text{MnO}_2$ ,  $\text{Fe}_2\text{O}_3$ ,  $\text{TiO}_2$ , and  $\text{CeO}_2$ ) were used for detection of  $\text{H}_2\text{O}_2$  [20-23]. Among them,  $\text{CeO}_2$  has been widely

used in biology, medicine and catalysis owing to its effective catalytic activity and free radical scavenging properties [24-26]. Particularly, the existence of a highly flowing lattice oxygen defect in the CeO<sub>2</sub> lattice contributed to the Ce<sup>3+</sup> and Ce<sup>4+</sup> conversion on the surface [27]. Besides, other properties like high surface area, biocompatibility, chemical stability, electrocatalytic and oxygen storage capacity significantly improve the performance of electrochemical sensors. Such as, Jha et al [28]. reported a novel synthesis approach of CeO<sub>2</sub>/reduced graphene oxide (rGO) xerogel composite to monitor H<sub>2</sub>O<sub>2</sub> by taking advantage of a sol-gel route consisting of CeO<sub>2</sub> nanoparticles anchored rGO nanosheets, which enhanced the detection performance towards H<sub>2</sub>O<sub>2</sub>. Wei Zhang and his colleagues [29] prepared Au/CeO<sub>2</sub>-chitsan composite films by one-step synthesis approach for H<sub>2</sub>O<sub>2</sub> sensing. The composite films show excellent response to H<sub>2</sub>O<sub>2</sub> and high stability. Although tremendous efforts have been made in H<sub>2</sub>O<sub>2</sub> electrochemical sensors, the selectivity and sensitivity of the existing materials still need to be improved.

In an attempt to address such difficulty of electrocatalytic performance of sensor device, two major issues have been considered. Firstly, a homeotypic bi-metallic co-existing material with two metals evenly distributed are required to observe their synergistic effect compared with other complex metal oxides. Secondly, porous material is expected to improve substantially the electrochemical performance and efficiency of the electrocatalytic device. Porous materials have well-defined channel connectivity, which could be

beneficial to shorten diffusion path and increase mass transfer efficiency. Moreover, porous material provides more effective surface area for electrochemical reaction, and allow better reaction kinetics at the electrode surface. However, to our best knowledge, there are few reports on the preparation of porous homeotypic bi-metallic co-existing oxide layers so far. Therefore, exploration of facile method is the key point for the fabrication of porous homeotypic bi-metallic co-existing oxide material. We notice that the metal-organic frameworks (MOFs) are the classic materials with highly order porous, metal sites, and ultrahigh surface area. Moreover, the synthesis of metal-based functional materials derived from MOFs precursors has also drawn great attention from researchers worldwide [30]. The materials derived from MOF precursors will inherit properties of MOFs, implying that MOFs is a promising precursor to prepare porous homeotypic bi-metallic co-existing oxide.

In this work, a series of mono-metallic and homeotypic bi-metallic co-existing materials ( $Ce_{1-x}Tb_xO_y$ ) were prepared by controlling the thermal decomposition conditions of  $Ce_{1-x}Tb_x$ -MOF precursor, and the resulted new porous materials were applied for preparation of selective chemical sensors towards  $H_2O_2$ .

## **2. Experimental**

### **2.1 Materials and Chemicals**

Cerium (III) nitrate hexahydrate ( $Ce(NO_3)_3 \cdot 6H_2O$ ), terbium nitrate hexahydrate ( $Tb(NO_3)_3 \cdot 6H_2O$ ), N, N-dimethylformamide (DMF), sodium acetate anhydrous

(CH<sub>3</sub>COONa), hydrogen peroxide (H<sub>2</sub>O<sub>2</sub>, 30%, w/w), 1,3,5-Benzenetricarboxylic acid (BTC) were purchased from Fluka. Sodium phosphate (NaH<sub>2</sub>PO<sub>4</sub>·2H<sub>2</sub>O and Na<sub>2</sub>HPO<sub>4</sub>·12H<sub>2</sub>O), chitosan (C<sub>6</sub>H<sub>11</sub>NO<sub>4</sub>)<sub>n</sub> and glutaraldehyde solution (C<sub>5</sub>H<sub>8</sub>O<sub>2</sub>, 25%, w/w) were purchased from Sinopharm Chemical Reagent Co., Ltd. All chemicals were used without further purification.

## 2.2 Preparation of Ce<sub>1-x</sub>Tb<sub>x</sub>-MOF crystals

Ce<sub>1-x</sub>Tb<sub>x</sub>-MOF crystals were synthesized following the procedure, according to our previous reports [31]. In a typical synthesis for the Ce<sub>0.9</sub>Tb<sub>0.1</sub>-MOF material, Cerium (III) nitrate hexahydrate (46.8 mg), terbium nitrate hexahydrate (5.4 mg) and Trimesic acid (H<sub>3</sub>BTC) (20 mg,) were dissolved in 10mL of Dimethylformamide (DMF) and 2 mL of deionized water. Then solution was added into Sodium Acetate (CH<sub>3</sub>COONa) (25 mg) under vigorous stirring at ambient temperature (~25 °C) for 10 min resulting in white crystals with a crystalline yield of 76% (based on H<sub>3</sub>BTC). The products were isolated by repeated centrifugation and washing with deionized water and DMF for several times. Finally, the products were dried in air at 60 °C.

## 2.3 Preparation of Ce<sub>1-x</sub>Tb<sub>x</sub>O<sub>y</sub> crystals

The Ce<sub>1-x</sub>Tb<sub>x</sub>O<sub>y</sub> crystals were prepared by pyrolysis of the as-synthesized Ce<sub>1-x</sub>Tb<sub>x</sub>-MOF crystals at 400 °C in air for 2 hours with a heating rate of 2 °C/min (the framework of the Ce<sub>1-x</sub>Tb<sub>x</sub>-MOF crystals begins to collapse at 350 °C).

## 2.4 Preparation of Ce<sub>1-x</sub>Tb<sub>x</sub>O<sub>y</sub>-modified glassy carbon electrode (GCE)

In order to study the electrochemical behaviour of the Ce<sub>1-x</sub>Tb<sub>x</sub>O<sub>y</sub> crystals, they were

deposited on a bare glassy carbon electrode (GCE). The GCE were pre-treated by polishing with a slurry of 0.05 mm alumina particles in order to create a mirror finish surface, and then sonicated in absolute ethanol and de-ionized water for 5 min. The GCE was rinsed thoroughly with de-ionized water and then dried at ambient temperature. Biopolymer chitosan (CHT) was used as an immobilization matrix to attach the  $Ce_{1-x}Tb_xO_y$  crystals on the GCE surface. A mixture of chitosan and  $Ce_{1-x}Tb_xO_y$  crystals was prepared by adding 10 mg  $Ce_{1-x}Tb_xO_y$  in 0.5 L chitosan (0.25% prepared in 0.1 M acetic acid), and then subjected to ultrasonic agitation for 30 min. The  $Ce_{1-x}Tb_xO_y$  crystals were prepared from the  $Ce_{1-x}Tb_x$ -MOF precursor (see previous section). 10  $\mu$ L of this mixture was cast onto the GCE surface and subjected to drying. Then the electrode was incubated with 2.5% glutaraldehyde for 10 min to crosslink the chitosan in order to increase the stability of the layer. The electrode was thoroughly rinsed with distilled water and dried in air to use.

## 2.5 Characterization

The structure and morphology of the as-prepared samples were characterized with a field emission scanning electron microscope (SEM) (Hitachi Limited S-4800 operating at 5 kV and JEOL JSM-7900F operating at 0.8 kV. High-resolution transmission electron microscopy (HRTEM) and the corresponding energy dispersive spectroscopy (EDS) mapping analyses were performed using a JEOL JEM-2100F microscope at an acceleration voltage of 200 kV. The powder X-ray diffraction (PXRD) patterns were collected on a Siemens D5005 diffractometer with Cu  $K\alpha$  radiation ( $\lambda = 1.5418 \text{ \AA}$ ). The infrared spectra (IR)

were measured with a NEXUS FT-IR using the KBr technique. Thermal gravimetric analysis (TGA) was performed on a Perkin-Elmer TGA thermogravimetric analyser in the temperature range of 25~800 °C under nitrogen atmosphere with a heating rate of 10 °C/min. N<sub>2</sub> adsorption/desorption isotherms were recorded at -196 °C on an ASAP 2020 Micromeritics instrument (before measurement, all samples were degassed at 200 °C overnight). X-ray photoelectron spectrum (XPS) analysis was carried out using a PH 5000 Versaprobe system using monochromatic Al K $\alpha$  radiation ( $h\nu = 1486.6$  eV). All binding energies were calibrated using the C 1s peak (284.8 eV). The electrochemical tests were carried out *via* an electrochemical analyzer (CHI660D, Chen hua, China). A conventional three-electrode cell was used with a saturated calomel electrode (SCE, saturated KCl) as a reference electrode, a platinum wire as counter electrode, and a bare or modified GCE (2 mm in diameter) as working electrode. Freshly prepared phosphate buffer (PB, 0.1 M, pH 7.4~8) solution was used as the supporting electrolyte. All electrochemical studies were performed under nitrogen atmosphere.

## 2.6 Theoretical Calculations

Theoretical calculations were performed using Vienna ab initio simulation packages (VASP) based on density functional theory (DFT) [32]. The core and valence electrons were described by the projector augmented wave (PAW) pseudopotentials. The generalized gradient approximation (GGA) proposed by Perdew, Burke, and Ernzerhof (PBE) was adopted to express the exchange correlation interactions with a cutoff energy

of 400 eV, while the van der Waals effect was accounted by the DFT-D2 method of Grimme with a 50 Å cutoff radius for pair interactions [33,34]. The fully relaxed lattice constants  $a = 5.41$  Å,  $b = 5.41$  Å and  $c = 5.41$  Å for CeO<sub>2</sub>. A  $2 \times 2 \times 3$  supercell with a 15 Å vacuum region was used to simulate the adsorption. The convergence of energy and forces were set to  $1 \times 10^{-4}$  eV and  $0.02$  eV Å<sup>-1</sup>, respectively. The Brillouin zone was sampled by the Monkhorst-Pack method with a  $3 \times 3 \times 1$  k-point grid. The adsorption energy is defined as  $\Delta E = E_{(\text{substrate} + \text{adsorbate})} - E_{\text{substrate}} - E_{\text{adsorbate}}$ . The formation energy of oxygen vacancy was calculated by the following equation:  $E_f = E_{\text{tot}}^p - E_{\text{tot}}^o + \mu_o$  where  $E_{\text{tot}}^p$  and  $E_{\text{tot}}^o$  are total energy of the pristine supercell and the supercell with O vacancy, respectively;  $\mu_o$  is the chemical potential of isolated oxygen atom.

### 3. Results and discussion

#### 3.1 Properties of Ce<sub>1-x</sub>Tb<sub>x</sub>-MOF crystals

For the preparation of homeotypic bi-metallic MOF (Ce<sub>1-x</sub>Tb<sub>x</sub>-MOF crystals), lanthanides metals (Ce and Tb) were selected. The Ce<sub>1-x</sub>Tb<sub>x</sub>-MOF crystals further used as a precursor is constructed from Ce and/or Tb and a rigid organic linker BTC through coordination bonding (Fig. 1). The Ce<sub>1-x</sub>Tb<sub>x</sub>-MOF has a tri-dimensional framework with a space group  $P4_322$ . Each building unit contains one seven-coordinated lanthanide ion (Ce and/or Tb), one BTC ligand and one water molecule; the lanthanide ion is coordinated with six oxygen atoms from six carboxylate groups of BTC ligands and one oxygen atom from a terminal water molecule (Fig. S1a) [35].

The homeotypic bi-metallic  $Ce_{1-x}Tb_x$ -MOF crystal structure was confirmed by XRD (Fig. S1b). The  $Ce_{0.9}Tb_{0.1}$ -MOF is representative of the  $Ce_{1-x}Tb_x$ -MOF series samples in this manuscript. The XRD diffraction peaks of the  $Ce_{0.9}Tb_{0.1}$ -MOF sample correspond to the mono-metallic Ce-MOF structure, in addition, no other crystal phase is detected. From the SEM picture of  $Ce_{0.9}Tb_{0.1}$ -MOF (Fig. S1d), highly dispersed and uniform micronsized rod-shaped crystals with a length and width of  $3\mu m$  and  $500\text{ nm}$ , respectively are seen. The size of the  $Ce_{0.9}Tb_{0.1}$ -MOF is comparable with the Ce-MOF (Fig. S1c).

### 3.2 Properties of $Ce_{1-x}Tb_xO_y$ crystals

The  $Ce_{0.9}Tb_{0.1}O_y$  crystals prepared from the  $Ce_{0.9}Tb_{0.1}$ -MOF precursor under pyrolysis at  $400\text{ }^\circ\text{C}$  in air atmosphere were characterized by XRD. As shown in Fig. 2a, the peaks at  $28.5^\circ$ ,  $33.2^\circ$ ,  $47.6^\circ$ ,  $56.4^\circ$ ,  $59.1^\circ$  and  $69.5^\circ$   $2\theta$  correspond to the (111), (200), (220), (311), (222), and (400) planes of  $CeO_2$ , which indicates that the  $Ce_{0.9}Tb_{0.1}$ -MOF precursor has been fully transformed to  $Ce_{0.9}Tb_{0.1}O_y$  [36,37]. The XRD pattern of  $Ce_{0.9}Tb_{0.1}O_y$  is exactly the same as for the  $CeO_2$  (Fig. S3a) implying that the bi-metallic crystals have been inherited from the MOF precursor. The similar properties of homeotypic elements such as atomic radius, number and weight result in highly stable  $Ce_{0.9}Tb_{0.1}O_y$  framework.

The transformation process from  $Ce_{0.9}Tb_{0.1}$ -MOF to  $Ce_{0.9}Tb_{0.1}O_y$  was followed by FT-IR and TGA. The IR spectrum of  $Ce_{0.9}Tb_{0.1}$ -MOF (Fig. S1e) contains three peaks including asymmetric stretching vibration of the carboxyl group at  $1590\sim 1480\text{cm}^{-1}$ , symmetric stretching vibration of the carboxyl group at  $1381\text{cm}^{-1}$

<sup>1</sup>, and C-C vibration of the aromatic ring at 1441 cm<sup>-1</sup>. These peaks disappear in the Ce<sub>0.9</sub>Tb<sub>0.1</sub>O<sub>y</sub> sample (Fig. S4a), indicating that Ce<sub>0.9</sub>Tb<sub>0.1</sub>-MOF skeleton structure collapsed [38]. In addition, the stretching vibration of Ce-O and Tb-O bonds at 556 cm<sup>-1</sup> originating from the Ce<sub>0.9</sub>Tb<sub>0.1</sub>-MOF can be clearly observed in Fig. S1e. This peak completely disappeared after pyrolysis, which demonstrates that the Ce<sub>0.9</sub>Tb<sub>0.1</sub>-MOF has been completely transformed to Ce<sub>0.9</sub>Tb<sub>0.1</sub>O<sub>y</sub> [39]. The thermal properties of Ce<sub>0.9</sub>Tb<sub>0.1</sub>-MOF were characterized by TG, as shown in Fig. S4b. Sample Ce<sub>0.9</sub>Tb<sub>0.1</sub>-MOF exhibits two weight losses in the temperature range 50~600 °C, corresponding to the weight loss (19.2 - 21.0%) attributed to the loss of physically absorbed water below 180 °C, and the weight loss (33 - 38%) due to the decomposition of the organic ligand (BTC) in the temperature range 350~400 °C. After decomposition, the remaining material is Ce<sub>0.9</sub>Tb<sub>0.1</sub>O<sub>y</sub>. The thermogravimetric analysis shows that the Ce<sub>x</sub>Tb<sub>1-x</sub>-MOF crystals have great thermal stability. The CeO<sub>2</sub> has similar properties to the Ce<sub>0.9</sub>Tb<sub>0.1</sub>O<sub>y</sub> as shown by FT-IR (Fig. S3b) and TG (Fig. S3c) characterizations.

The SEM pictures of Ce<sub>0.9</sub>Tb<sub>0.1</sub>O<sub>y</sub> crystals are presented in Fig. 2b. The rod-like morphology of the Ce<sub>0.9</sub>Tb<sub>0.1</sub>O<sub>y</sub>-MOF precursor is well preserved after heat treatment. The crystals length and width are 2 μm and 250 nm, respectively. In comparison to the Ce<sub>0.9</sub>Tb<sub>0.1</sub>-MOF precursor (Fig. S1d), the Ce<sub>0.9</sub>Tb<sub>0.1</sub>O<sub>y</sub> crystals decrease in size, moreover, they contain visible pores of 100 nm located on the particles surface (Fig. S2). It can be speculated that in the initial stage of pyrolysis, uniform nanoparticles of bi-metallic oxide with the organic ligand (BTC) are

formed. Subsequently, these unstable bi-metallic oxide nanoparticles are aggregated and formed micronsized  $\text{Ce}_{0.9}\text{Tb}_{0.1}\text{O}_y$  crystals (Ostwald ripening) with a large number of holes appearing on their surface. Based on the above results, the formation mechanism of the porous micronsized  $\text{Ce}_{0.9}\text{Tb}_{0.1}\text{O}_y$  is proposed, and it proceeds *via* a two-step process, as depicted in Fig. 2e. As shown, large amount of high-energy unstable bi-metallic oxide nanoparticles were obtained within a very short time (Fig. 2e: step 1). Due to the Ostwald ripening, these nanoparticles continuously aggregate into micronsized 3D superstructures (Fig. 2e: step 2). Most importantly, mesopores and macropores are formed during the formation of the bi-metallic oxide, which could be beneficial to shorten diffusion path and increase mass transfer efficiency. Moreover, the porous structure of the bi-metallic oxides would provide more effective surface area for electrochemical reaction, and will allow faster reaction kinetics at the electrode surface. SEM (Fig. S3e) and TEM (Fig. S3f) pictures of  $\text{CeO}_2$  show great similarities to sample  $\text{Ce}_{0.9}\text{Tb}_{0.1}\text{O}_y$ .

The  $\text{N}_2$  isotherm (Fig. 2c) recorded from the  $\text{Ce}_{0.9}\text{Tb}_{0.1}\text{O}_y$  sample is a Type-IV with a H3-type hysteresis loop, which is indicative for the presence of meso- and macro-pores in the crystals. These results are consistent with SEM analysis. A detailed comparison of samples  $\text{Ce}_{0.9}\text{Tb}_{0.1}\text{O}_y$  and  $\text{CeO}_2$  is presented in Table S2. The surface area and pore volume for  $\text{Ce}_{0.9}\text{Tb}_{0.1}\text{O}_y$  are  $105 \text{ m}^2 \cdot \text{g}^{-1}$  and  $0.12 \text{ cm}^3 \cdot \text{g}^{-1}$ , respectively. In comparison, the surface area and pore volume of  $\text{CeO}_2$  are  $94 \text{ m}^2 \cdot \text{g}^{-1}$  of  $0.11 \text{ cm}^3 \cdot \text{g}^{-1}$ , respectively. The bi-metallic  $\text{Ce}_{0.9}\text{Tb}_{0.1}\text{O}_y$  sample shows

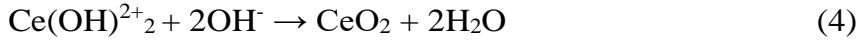
slightly higher surface area and pore volume in comparison to the  $\text{CeO}_2$ , which is expected to provide more accessible catalytic sites and easier diffusion. The scanning transmission electron microscope (STEM) and energy-dispersive X-ray spectroscopy (EDS) images (Fig. 2d) reveal that O, Ce, and Tb are homogeneously distributed within the  $\text{Ce}_{0.9}\text{Tb}_{0.1}\text{O}_y$  crystals. The Ce/Tb ratio of 9:1 for the bulk sample is derived from the EDS.

The chemical state of the components in both samples ( $\text{Ce}_{0.9}\text{Tb}_{0.1}\text{O}_y$  and  $\text{CeO}_2$ ) was investigated by XPS. In Fig. 3a, the binding energy of Ce  $3d_{5/2}$  peak for the  $\text{Ce}_{0.9}\text{Tb}_{0.1}\text{O}_y$  is located at 881.38, 887.6, and 897.4 eV, while the corresponding binding energy for the  $\text{CeO}_2$  is measured at 882.3, 888.1, and 898.4 eV. As shown, the binding energy for the  $\text{Ce}_{0.9}\text{Tb}_{0.1}\text{O}_y$  crystals obviously decrease. The systematic energy shift due to the electronic cloud density increase, indicating that in the preparation process of  $\text{Ce}_{0.9}\text{Tb}_{0.1}\text{-MOF}$ , the Tb indeed enter into the  $\text{La-(1, 3, 5-BTC)(H}_2\text{O)}_6$  lattice. After heat-treatment, the Ce and Tb coexist in the oxide crystals by chemical bonding instead of mechanical mixing of two oxides. Moreover, the high-resolution spectrum of Ce 3d contains two peaks corresponding to  $\text{Ce}^{3+}$  (u) and  $\text{Ce}^{4+}$  (v) [40]. The  $\text{Ce}^{3+}$  content in samples  $\text{CeO}_2$  and  $\text{Ce}_{0.9}\text{Tb}_{0.1}\text{O}_y$  is 31% and 40%, respectively. Three peaks at 528.6, 530.8, and 532.5 eV labelled as  $\text{Q}_L$ ,  $\text{Q}_V$ , and  $\text{Q}_A$  are appeared in the  $\text{Ce}_{0.9}\text{Tb}_{0.1}\text{O}_y$  O1s XPS spectrum, which can be attributed to lattice oxygen, oxygen, and surface-adsorption species (Fig. 3b) [45.46]. The corresponding binding energy for  $\text{CeO}_2$  is primarily centered at 529.3, 531.2, and 532.7 eV. The binding energy of  $\text{Ce}_{0.9}\text{Tb}_{0.1}\text{O}_y$  exhibits obvious decrease in comparison with  $\text{CeO}_2$ . Apparently, the relative

percentages of Ov in the  $\text{Ce}_{0.9}\text{Tb}_{0.1}\text{O}_y$  crystal (20%) is higher than that in the  $\text{CeO}_2$  crystal (15%). The  $\text{Ce}^{3+}$  keep the electrostatic equilibrium and produce flowing lattice oxygen defects, namely, the  $\text{Ce}^{3+}$  can accelerate the electron transfer rate and thus improve the electrochemical activity [41]. Notably, the  $\text{Ce}^{3+}$  content in the  $\text{Ce}_{0.9}\text{Tb}_{0.1}\text{O}_y$  is more than that in the  $\text{CeO}_2$ . It demonstrates that the Tb ions can attribute to produce  $\text{Ce}^{3+}$ . Therefore, it is expected that the  $\text{Ce}_{0.9}\text{Tb}_{0.1}\text{O}_y$  will be more efficient than the  $\text{CeO}_2$  in electrochemical reactions.

### 3.3 Electrochemical activity of $\text{Ce}_{1-x}\text{Tb}_x\text{O}_y$ toward $\text{H}_2\text{O}_2$

The influence of the Ce/Tb ratio of the materials on electrochemical performance was studied by cyclic voltammetry. The  $\text{Ce}_{0.9}\text{Tb}_{0.1}\text{O}_y$  modified GCE (sample abbreviated as GCE- $\text{Ce}_{0.9}\text{Tb}_{0.1}\text{O}_y$ ), shows the strongest redox peak (Fig. S5), and the redox peak decreases gradually along with the increase of the Tb content. The cyclic voltammetry results show that the Ce/Tb ratio of 0.9 is optimal for  $\text{H}_2\text{O}_2$  detection. Therefore, the  $\text{Ce}_{0.9}\text{Tb}_{0.1}\text{O}_y$  crystals were selected for further electrochemical characterization. The cyclic voltammetry (CV) curves for the three samples, *i.e.*, blank GCE, GCE- $\text{CeO}_2$ , and GCE- $\text{Ce}_{0.9}\text{Tb}_{0.1}\text{O}_y$  before and after addition of 10 mM  $\text{H}_2\text{O}_2$  are depicted in Fig. 4a and b. All three samples do not show any redox peak in phosphate buffered solution (PBS) prior addition of  $\text{H}_2\text{O}_2$ . After adding the  $\text{H}_2\text{O}_2$ , the reference electrode (GCE) shows a weak peak at 0.9 V. While the GCE- $\text{CeO}_2$  sample (Fig. 4a) exhibits a wide peak at 0.45 V representative for the detection of  $\text{H}_2\text{O}_2$ . The surface reaction process can be represented by the following equations [42-44],



In comparison, the GCE-Ce<sub>0.9</sub>Tb<sub>0.1</sub>O<sub>y</sub> shows a wide peak at same potential point (Fig. 4b) but the peak current increases by 60%, which can be attributed to that the synergy of Tb and Ce leading to improved detection. To evaluate the detection limit, sensitivity, and the linear range of the GCE-Ce<sub>0.9</sub>Tb<sub>0.1</sub>O<sub>y</sub>, the measurements were performed with different concentration of H<sub>2</sub>O<sub>2</sub>; the amperometric response at 0.75V in 0.1 M PBS solution with continuous addition of H<sub>2</sub>O<sub>2</sub> was measured. The current value (95%) reach steady state within 8s, indicating that the sensor responds quickly to H<sub>2</sub>O<sub>2</sub>, and the current increases alone with the increase of the H<sub>2</sub>O<sub>2</sub> concentration (Fig. 4c-f). For the GCE-CeO<sub>2</sub>, the linear range is 0.2 to 4.2 mM (the calculated curve is  $I_{\text{Pa}} (\mu\text{A}) = 0.7748 C (\text{mM}) + 0.4237$  ( $R^2 = 0.9991$ )), the sensitivity is  $0.7748 \mu\text{A} \cdot \text{mM}^{-1}$  ( $6.17 \mu\text{A} \cdot \text{mM}^{-1} \cdot \text{cm}^{-2}$ ,  $R^2 = 0.9991$ ), and the detection limit is  $17 \mu\text{M}$  ( $S/N = 3$ ) (Fig. 4c and d). The amperometric response of the GCE-Ce<sub>0.9</sub>Tb<sub>0.1</sub>O<sub>y</sub> is shown in Fig. 4e and f. The current intensity for the GCE-Ce<sub>0.9</sub>Tb<sub>0.1</sub>O<sub>y</sub> is 1.5 times higher than for the GCE-CeO<sub>2</sub>. The linear range, sensitivity and detection limit are 0.1 to 4.2 mM ( $I_{\text{Pa}} (\mu\text{A}) = 1.6318 C (\text{mM}) + 2.012$  ( $R^2 = 0.9999$ )),  $1.6318 \mu\text{A} \cdot \text{mM}^{-1}$  ( $12.99 \mu\text{A} \cdot \text{mM}^{-1} \cdot \text{cm}^{-2}$ ,  $R^2 = 0.9999$ ) and  $7.7 \mu\text{M}$  ( $S/N = 3$ ), respectively. The results

show that the GCE-Ce<sub>0.9</sub>Tb<sub>0.1</sub>O<sub>y</sub> has higher capacity towards H<sub>2</sub>O<sub>2</sub> detection in comparison to the GCE-CeO<sub>2</sub>. An evaluation of the performance of the current sensor (GCE-Ce<sub>0.9</sub>Tb<sub>0.1</sub>O<sub>y</sub>) with those described in the literature is presented in Table S3. The sensitivity, detection limit and linear range of the GCE-Ce<sub>0.9</sub>Tb<sub>0.1</sub>O<sub>y</sub> sensor for H<sub>2</sub>O<sub>2</sub> are higher in comparison with those reported in the open literature. The great performance of the GCE-Ce<sub>0.9</sub>Tb<sub>0.1</sub>O<sub>y</sub> sensor for H<sub>2</sub>O<sub>2</sub> is due to the following two reasons: Firstly, the Tb in the La-(1, 3, 5-BTC) H<sub>2</sub>O)<sub>6</sub> structure is chemically bonded and thus lead to synergy between Ce and Tb in the Ce<sub>0.9</sub>Tb<sub>0.1</sub>-MOF. After pyrolysis, the Ce<sub>0.9</sub>Tb<sub>0.1</sub>O<sub>y</sub> inherited the synergy between Ce and Tb from MOFs precursor. It can produce more Ce<sup>3+</sup>, and increases the concentration of oxygen vacancies in the lattice, thus accelerating the conduction rate of the charge, which promotes the electrode surface rapid catalytic reaction. Secondly, the uniform crystals in size with regular pores are beneficial to shorten diffusion path and increase mass transfer efficiency. Thus the porous Ce<sub>0.9</sub>Tb<sub>0.1</sub>O<sub>y</sub> crystals provide more effective surface area for electrochemical reaction, and allow faster reaction kinetics at the electrode surface.

The Fig. S6a shows a response curve of CV (Cyclic Voltammetry) measurements in 10 Mm H<sub>2</sub>O<sub>2</sub> solution. All curves coincide well after 30 cycles sweep in the voltage range of -1.5V-1.5V, indicating that GCE-Ce<sub>0.9</sub>Tb<sub>0.1</sub>O<sub>y</sub> shows high stability for H<sub>2</sub>O<sub>2</sub>. In addition, the selectivity of GCE-Ce<sub>0.9</sub>Tb<sub>0.1</sub>O<sub>y</sub> was tested. 0.3 mM H<sub>2</sub>O<sub>2</sub>, 0.1 mM glucose, 0.3 mM H<sub>2</sub>O<sub>2</sub>, 0.1 mM ascorbic acid,

0.3 mM H<sub>2</sub>O<sub>2</sub>, 0.1 mM urea, 0.3 mM H<sub>2</sub>O<sub>2</sub>, 0.1 mM sucrose, 0.3 mM H<sub>2</sub>O<sub>2</sub>, and 0.1 mM citric acid were sequentially added during the amperometric test. From Fig. S6b it can be seen that response current generated by adding H<sub>2</sub>O<sub>2</sub> is obvious. However, response current is weak and the interference can be ignored when others substance was injected into PBS, indicating that GCE-Ce<sub>0.9</sub>Tb<sub>0.1</sub>O<sub>y</sub> exhibited good selectivity for H<sub>2</sub>O<sub>2</sub>.

Further understanding of the intrinsic property and reactivity of Ce<sub>0.9</sub>Tb<sub>0.1</sub>O<sub>y</sub> crystals together with the adsorption phenomena of the H<sub>2</sub>O<sub>2</sub> were studied by density functional theory (DFT). The most thermodynamically stable (111) surface was selected and presented in Fig. S7. While all possible active sites were investigated and show in Fig. S8. Compared with pure CeO<sub>2</sub> model, the adsorption energy of H<sub>2</sub>O<sub>2</sub> on Ce<sub>0.9</sub>Tb<sub>0.1</sub>O<sub>y</sub> model decrease from -0.99 eV to -2.48 eV, and the O-H band of H<sub>2</sub>O<sub>2</sub> increases from 1.01 Å to 1.59 Å, indicating that the adsorption of H<sub>2</sub>O<sub>2</sub> is more favorable on Ce<sub>0.9</sub>Tb<sub>0.1</sub>O<sub>y</sub> model (Fig. 5a and b). The larger absolute adsorption energy for H<sub>2</sub>O<sub>2</sub> on Ce<sub>0.9</sub>Tb<sub>0.1</sub>O<sub>y</sub> model prove the detected substance is more easily adsorbed on the adsorbent, and the electrode material has higher sensitivity and lower detection limit to the substance H<sub>2</sub>O<sub>2</sub>. Our calculations agree well with the experimental results. When Ce is substituted by Tb possessing higher electron negativity ( $x = 1.20$ ) than that of Ce ( $x = 1.12$ ), thus Ce can readily donate more electrons to the O atoms, yielding some electron-positivity and electron-negativity cations on Ce and O, respectively (Fig. S9). This result was further confirmed by Bader analysis. As a result, the O and H atom of H<sub>2</sub>O<sub>2</sub> can favor asorbtion on the neighbor Ce and O surrounding Tb, respectively. The

DFT calculations suggest that the synergistic effect between Ce and Tb can further trigger the intrinsic activity of the as-prepared  $\text{Ce}_{0.9}\text{Tb}_{0.1}\text{O}_y$  electrodes. Moreover, Fig. 5c and d indicate that the  $\text{CeO}_2$  model with oxygen defects exhibits a narrow band gap of 1.25 eV in comparison with pristine  $\text{CeO}_2$  (1.93 eV), confirming the improvement of the intrinsic electron transfer capacity by introduction of  $\text{Ce}^{3+}$ . The formation energy of oxygen vacancy for  $\text{CeO}_2$  and  $\text{Ce}_{0.9}\text{Tb}_{0.1}\text{O}_y$  are -0.63 and -0.82 eV, respectively, indicating that the oxygen vacancy is facilitated by Tb incorporation (Fig. S10). These results prove the increased concentration of oxygen vacancies in the  $\text{Ce}_{0.9}\text{Tb}_{0.1}\text{O}_y$ , which is in agreement with XPS results shown above.

#### 4. Conclusion

Porous  $\text{Ce}_{1-x}\text{Tb}_x\text{O}_y$  crystals are prepared through direct pyrolysis of homeotypic bi-metallic  $\text{Ce}_{1-x}\text{Tb}_x\text{-MOF}$  precursors. The porous  $\text{Ce}_{1-x}\text{Tb}_x\text{O}_y$  crystals deposited on glassy carbon electrodes were used for detection of  $\text{H}_2\text{O}_2$  in alkaline solutions. The glassy carbon electrodes covered with  $\text{Ce}_{0.9}\text{Tb}_{0.1}\text{O}_y$  crystals exhibited high stability, high sensitivity toward  $\text{H}_2\text{O}_2$  ( $1.6831 \mu\text{A}\cdot\text{Mm}^{-1}$ ) ( $12.99 \mu\text{A}\cdot\text{mM}^{-1}\cdot\text{cm}^{-2}$ ) in a broad linear range (0.1  $\mu\text{M}$  - 4.2 mM) with a detection limit of 7.7  $\mu\text{M}$  ( $S/N = 3$ ), and fast response (less than 10 s). The synergy between Tb and Ce proves the detected substance is more easily adsorbed on the adsorbent, which enhances the electrochemical behaviour remarkably. Besides, the well-defined pores connectivity attributed to the improved reaction efficiency. This new concept presented here paves the way to efficient sensing of  $\text{H}_2\text{O}_2$  using porous homeotypic bi-metallic materials.

## Acknowledgements

The authors acknowledge the support from the National Natural Science Foundation of China (Grant No. 21201180, 21673291), the Shandong Provincial Natural Science Foundation (ZR2012BQ014), the Fundamental Research Funds for the Central Universities (No. 15CX05012A, 12CX04039A), and Qingdao Application of Basic Research Projects (No.14-2-4-36-jch).

## References

- [1] M.S. Lin, H.J. Leu, A  $\text{Fe}_3\text{O}_4$ -based chemical sensor for cathodic determination of hydrogen peroxide, *Electroanal.* 17 (2005) 2068-2073.
- [2] M. Abbas, W. Luo, L. Zhu, J. Zou, H. Tang, Fluorometric determination of hydrogen peroxide in milk by using a Fenton reaction system, *Food Chem.* 120 (2010) 327-331.
- [3] P. Tanner, A. Wong, Spectrophotometric determination of hydrogen peroxide in rainwater, *Anal. Chim. Acta* 370 (1998) 279-287.
- [4] A.N. Diaz, M.R. Peinado, M.T. Minguez, Sol-gel horseradish peroxidase biosensor for hydrogen peroxide detection by chemiluminescence, *Anal. Chim. Acta* 363 (1998) 221-227.
- [5] J. Lu, C. Lau, M. Morizono, K. Ohta, M. Kai, A chemiluminescence reaction between hydrogen peroxide and acetonitrile and its applications, *Anal. Chem.* 73 (2001) 5979-5983.
- [6] C.A. Marquette, L.J. Blum, Luminol electrochemiluminescence-based fibre optic biosensors for flow injection analysis of glucose and lactate in natural samples, *Anal. Chim. Acta* 381 (1999) 1-10.
- [7] G. Xu, S. Dong, Chemiluminescent determination of luminol and hydrogen peroxide using hematin immobilized in the bulk of a carbon paste electrode, *Electroanal.* 11 (1999) 1180-1184.
- [8] M.C. Chang, A. Pralle, E.Y. Isacoff, C.J. Chang, A selective, cell-permeable optical probe for hydrogen peroxide in living cells, *J. Am. Chem. Soc.* 126 (2004) 15392-15393.

- [9] N. Dasgupta, M.C. Wolfgang, A.L. Goodman, S.K. Arora, J. Jyot, S. Lory, R. Ramphal, A four-tiered transcriptional regulatory circuit controls flagellar biogenesis in *Pseudomonas aeruginosa*, *Mol. Microbiol.* 50 (2003) 809-824.
- [10] A. Sakuragawa, T. Tani, T. Okutani, Fluorometric determination of microamounts of hydrogen peroxide with an immobilized enzyme prepared by coupling horseradish peroxidase to chitosan beads, *Anal. Chim. Acta* 374 (1998) 191-200.
- [11] M. Zhou, Z. Diwu, N. Panchuk-Voloshina, R.P. Haugland, A stable nonfluorescent derivative of resorufin for the fluorometric determination of trace hydrogen peroxide: applications in detecting the activity of phagocyte NADPH oxidase and other oxidases, *Anal. Biochem.* 253 (1997) 162-168.
- [12] E. Hurdis, H. Romeyn, Accuracy of determination of hydrogen peroxide by cerate oxidimetry, *Anal. Chem.* 26 (1954) 320-325.
- [13] N.V. Klassen, D. Marchington, H.C. McGowan, H<sub>2</sub>O<sub>2</sub> determination by the I<sub>3</sub>-method and by KMnO<sub>4</sub> titration, *Anal. Chem.* 66 (1994) 2921-2925.
- [14] M.I. Awad, C. Harnode, K. Tokuda, T. Ohsaka, Simultaneous electroanalysis of peroxyacetic acid and hydrogen peroxide, *Anal. Chem.* 73 (2001) 1839-1843.
- [15] A.A. Karyakin, E.A. Puganova, I.A. Budashov, I.N. Kurochkin, E.E. Karyakina, V.A. Levchenko, V.N. Matveyenko, S.D. Varfolomeyev, Prussian blue based nanoelectrode arrays for H<sub>2</sub>O<sub>2</sub> detection, *Anal. Chem.* 76 (2004) 474-478.
- [16] L. Mao, P.G. Osborne, K. Yamamoto, T. Kato, Continuous on-line measurement of cerebral hydrogen peroxide using enzyme-modified ring-disk plastic carbon film electrode, *Anal. Chem.* 74 (2002) 3684-3689.
- [17] M. Delvaux, A. Walcarius, S. Demoustier-Champagne, Electrocatalytic H<sub>2</sub>O<sub>2</sub> amperometric detection using gold nanotube electrode ensembles, *Anal. Chim. Acta*, 525 (2004) 221-230.
- [18] E. Kurowska, A. Brzózka, M. Jarosz, G.D. Sulka, M. Jaskuła, Silver nanowire array sensor for sensitive and rapid detection of H<sub>2</sub>O<sub>2</sub>, *Electrochim. Acta* 104 (2013) 439-447.
- [19] D. Janasek, W. Vastarella, U. Spohn, N. Teuscher, A. Heilmann, Ruthenium/rhodium modified gold electrodes for the amperometric detection of hydrogen peroxide at low potentials, *Anal. Bioanal. Chem.* 374 (2002) 1267-1273.
- [20] A. Salimi, R. Hallaj, S. Soltanian, S. Soltanian, H. Mamkhezri, Nanomolar detection of hydrogen peroxide on glassy carbon electrode modified with electrodeposited cobalt oxide nanoparticles, *Anal. Chim. Acta.* 594 (2007) 24-31.

- [21] J. Hrbac, V. Halouzka, R. Zboril, K. Papadopoulos, T. Triantis, Carbon Electrodes Modified by Nanoscopic Iron(III) Oxides to Assemble Chemical Sensors for the Hydrogen Peroxide Amperometric Detection, *Electroanal.* 19 (2007) 1850-1854.
- [22] S. Yao, J. Xu, Y. Wang, X. Chen, Y. Xu, S. Hu, A highly sensitive hydrogen peroxide amperometric sensor based on MnO<sub>2</sub> nanoparticles and dihexadecyl hydrogen phosphate composite film, *Anal. Chim. Acta.* 557 (2006) 78-84.
- [23] M. Hermanek, R. Zboril, L. Medrik, J. Pechousek, C. Gregor, Catalytic Efficiency of Iron(III) Oxides in Decomposition of Hydrogen Peroxide: Competition between the Surface Area and Crystallinity of Nanoparticles, *J. Am. Chem. Soc.* 129 (2007) 10929-10936.
- [24] D. Schubert, R. Dargusch, J. Raitano, S.-W. Chan, Cerium and yttrium oxide nanoparticles are neuroprotective, *Biochem. Biophys. Res. Co.* 342 (2006) 86-91.
- [25] F. Pagliari, C. Mandoli, G. Forte, E. Magnani, S. Pagliari, G. Nardone, S. Licoccia, M. Minieri, P. Nardo, E. Traversal, Cerium oxide nanoparticles protect cardiac progenitor cells from oxidative stress, *ACS Nano* 6 (2012) 3767-3775.
- [26] J. Niu, K. Wang, P.E. Kolattukudy, Cerium oxide nanoparticles inhibits oxidative stress and nuclear factor- $\kappa$ B activation in H<sub>9c2</sub> cardiomyocytes exposed to cigarette smoke extract, *J. Pharmacol. Exp. Ther.* 338 (2011) 53-61.
- [27] M. Das, S. Patil, N. Bhargava, J.-F. Kang, L. Riedel, S. Seal, J. Hickman, Auto-catalytic ceria nanoparticles offer neuroprotection to adult rat spinal cord neurons, *Biomaterials* 28 (2007) 1918-1925.
- [28] S.K. Jha, C.N. Kumar, R.P. Raj, N. Jha, S. Mohan, Synthesis of 3D porous CeO<sub>2</sub>/reduced graphene oxide xerogel composite and low level detection of H<sub>2</sub>O<sub>2</sub>, *Electrochim. Acta* 120 (2014) 308-313.
- [29] W. Zhang, G. Xie, S. Li, L. Lu, B. Liu, Au/CeO<sub>2</sub>-chitosan composite film for hydrogen peroxide sensing, *App. Surf. Sci.* 258 (2012) 8222-8227.
- [30] B.Y. Guan, L.Yu, X.W. Lou, A dual-metal-organic-framework derived electrocatalyst for oxygen reduction, *Energy Environ. Sci.* 9 (2016) 3092-3096.
- [31] H. Guo, Y. Zhu, S. Qiu, J. Lercher, H. Zhang, Coordination modulation induced synthesis of nanoscale Eu<sub>1-x</sub>Tb<sub>x</sub>-metal-organic frameworks for luminescent thin films, *Adv. Mater.* 22 (2010) 4190-4192.
- [32] G. Kresse, J. Furthmüller, Efficient iterative schemes for ab initio total-energy calculations using a plane-wave basis set, *Phys. Rev. B: Condens. Matter Mater. Phys.* 54 (1996) 11169-11186.
- [33] J.P. Perdew, K. Burke, M. Ernzerhof, Generalized gradient approximation made simple, *Phys. Rev. Lett.* 77 (1996) 3865-3868.

- [34] S. Grimme, J. Antony, S. Ehrlich, H. Krieg, A consistent and accurate ab initio parametrization of density functional dispersion correction (DFT-D) for the 94 elements H-Pu, *J. Chem. Phys.* 132 (2010) 154104.
- [35] X. Guo, G. Zhu, Z. Li, F. Sun, Z. Yang, S. Qiu. A lanthanide metal-organic framework with high thermal stability and available Lewis-acid metal sites, *Chem. Comm.* 30 (2006) 3172.
- [36] K. Liu, G. Jia, Y. Zheng, Y. Song, M. Yang, Y. Huang, L. Zhang, H. You, Room-temperature synthesis and luminescence properties of  $\text{Eu}^{3+}/\text{Tb}^{3+}$ -doped  $\text{La}(1,3,5\text{-BTC})(\text{H}_2\text{O})_6$ , *Inorg. Chem. Commun.* 12 (2009) 1246-1249.
- [37] H-I. Chen, H-Y. Chang, Homogeneous precipitation of cerium dioxide nanoparticles in alcohol/water mixed solvents, *Colloid. Surface. A* 242 (2004) 61-69.
- [38] J. Yang, Q. Yue, G-D. Li, G-H. Li, J-S. Chen, Structures, photoluminescence, up-conversion, and magnetism of 2D and 3D rare-earth coordination polymers with multicarboxylate linkages, *Inorg. Chem.* 45 (2006) 2857-2865.
- [39] S.-L. Lin, C.-S. Hwang, Structures of  $\text{CeO}_2\text{-Al}_2\text{O}_3\text{-SiO}_2$  glasses, *Non-Cryst Solid* 202 (1996) 61-67.
- [40] F. Larachi, J. Pierre, A. Adnot, A. Bernis, Ce 3d XPS study of composite  $\text{Ce}_x\text{Mn}_{1-x}\text{O}_{2-y}$  wet oxidation catalysts, *Appl. Surf. Sci.* 195 (2002) 236-250.
- [41] Y. Su, Z. Tang, W. Han, P. Zhang, Y. Song, G. Lu, Influence of the pore structure of  $\text{CeO}_2$  supports on the surface texture and catalytic activity for CO oxidation, *CrystEngComm* 16 (2014) 5189-5197.
- [42] M. Das, S. Patil, N. Bhargava, J-F. Kang, L. Riedel, S. Seal, J. Hickman, Auto-catalytic ceria nanoparticles offer neuroprotection to adult rat spinal cord neurons, *Biomaterials*, 28 (2007) 1918-1925.
- [43] C. Ispas, J. Njagi, M. Cates, S. Andreescu, Electrochemical studies of ceria as electrode material for sensing and biosensing applications, *J. Electrochem. Soc.* 155 (2008) 169-176.
- [44] D. Schubert, R. Dargusch, J. Raitano, S-W. Chan, Cerium and yttrium oxide nanoparticles are neuroprotective, *Biochem. Bioph. Res. Co.* 342 (2006) 86-91.
- [45] G. Ming, Y.S Xu, B. Wen, R. Lin, B.H Ge, Y. Tang, Y.W. Liang, C. Yang, K. Huang, D. Zu, R. Yu, W.X. Chen, J. Li, H. Wu, L.M. Liu and Y.D. Li, Tuning defects in oxides at room temperature by lithium reduction, *Nat. Commun.*, 9 (2018) 1302.
- [46] J. Bao, X.D. Zhao, B. Fan, J.J. Zhang, M. Zhou, W. L. Yang, B.C. Pan, and Y. Xie,

ultrathin spinel-structured nanosheets rich in oxygen deficiencies for enhanced electrocatalytic water oxidation, *Angew. Chem.*, 127 (2015) 7507-75.



**Fig. 1.** Schematic representation of synthetic route used for preparation of  $Ce_{0.9}Tb_{0.1}O_y$  from  $Ce_{1-x}Tb_x$  -MOF by pyrolysis, followed by their use for detection of  $H_2O_2$ .

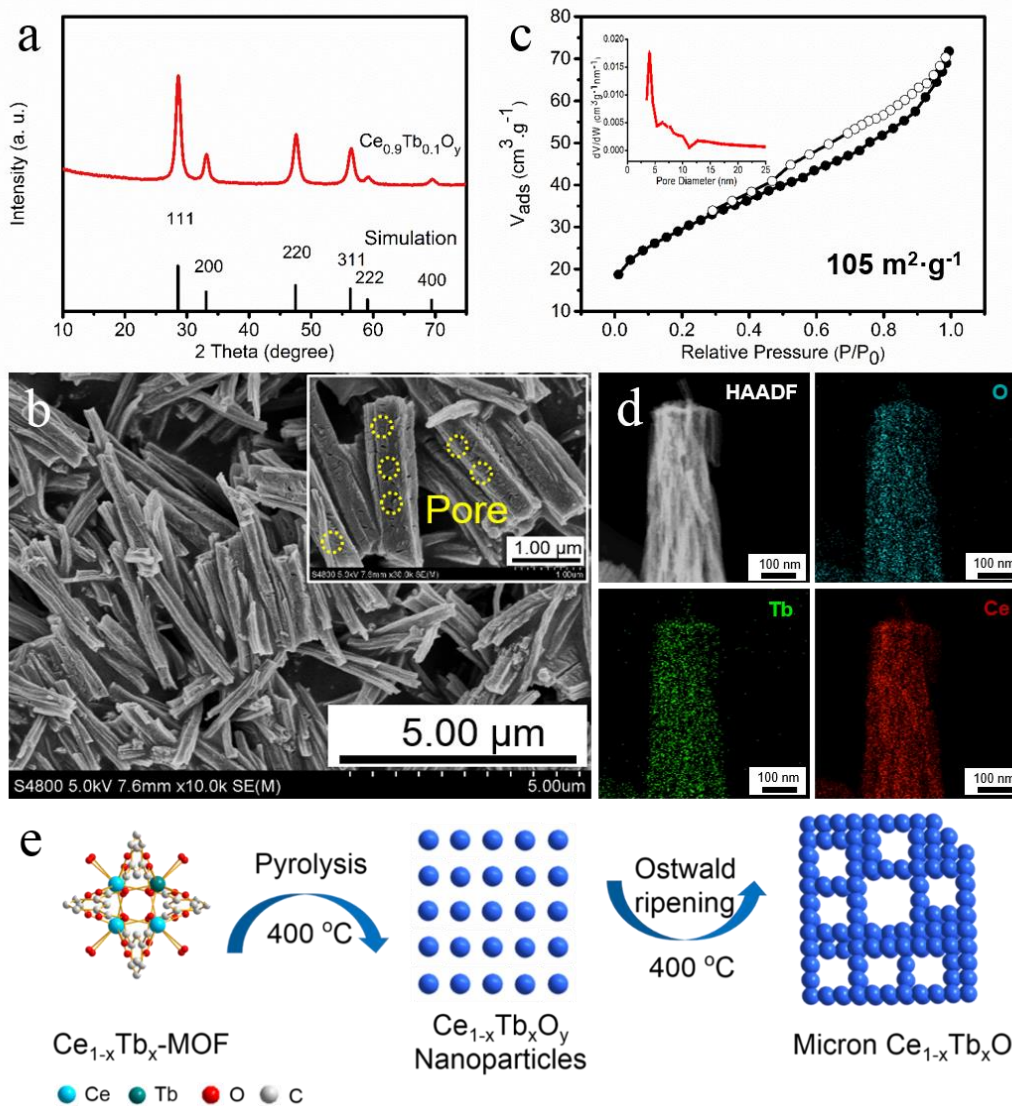


**Fig. 2.** a, XRD patterns of  $\text{Ce}_{0.9}\text{Tb}_{0.1}\text{O}_y$ ; b, SEM picture of  $\text{Ce}_{0.9}\text{Tb}_{0.1}\text{O}_y$ ; c,  $\text{N}_2$  sorption isotherm at 77K (Inset: pore size distribution of  $\text{Ce}_{0.9}\text{Tb}_{0.1}\text{O}_y$ ); d, HAADF-STEM and EDS images O (Blue), Ce (Red), Tb (Green) of  $\text{Ce}_{0.9}\text{Tb}_{0.1}\text{O}_y$ ; e, Proposed pathway for the formation of the  $\text{Ce}_{1-x}\text{Tb}_x\text{O}_y$  porous structure by pyrolysis of the  $\text{Ce}_{1-x}\text{Tb}_x\text{-MOF}$ .

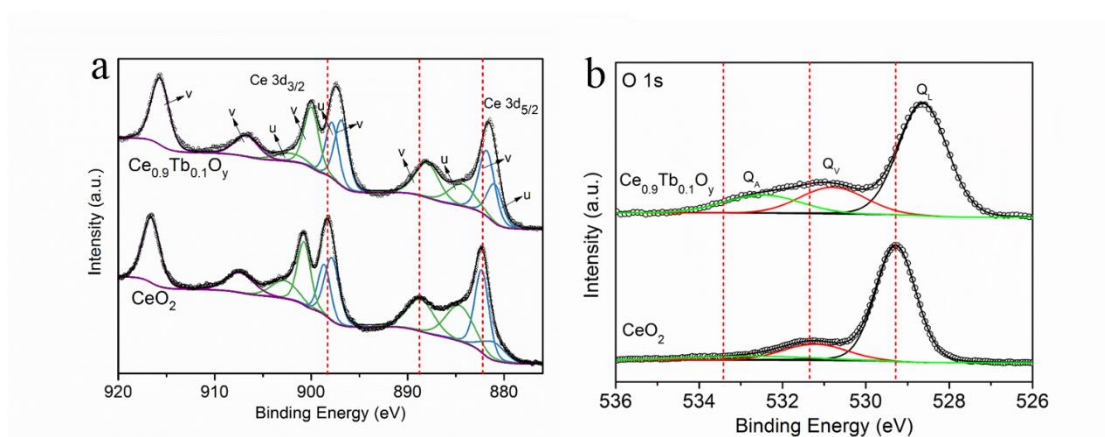


**Fig. 3.** XPS spectra of a, Ce 3d and b, O 1s for samples  $\text{CeO}_2$  and  $\text{Ce}_{0.9}\text{Tb}_{0.1}\text{O}_y$ , respectively.

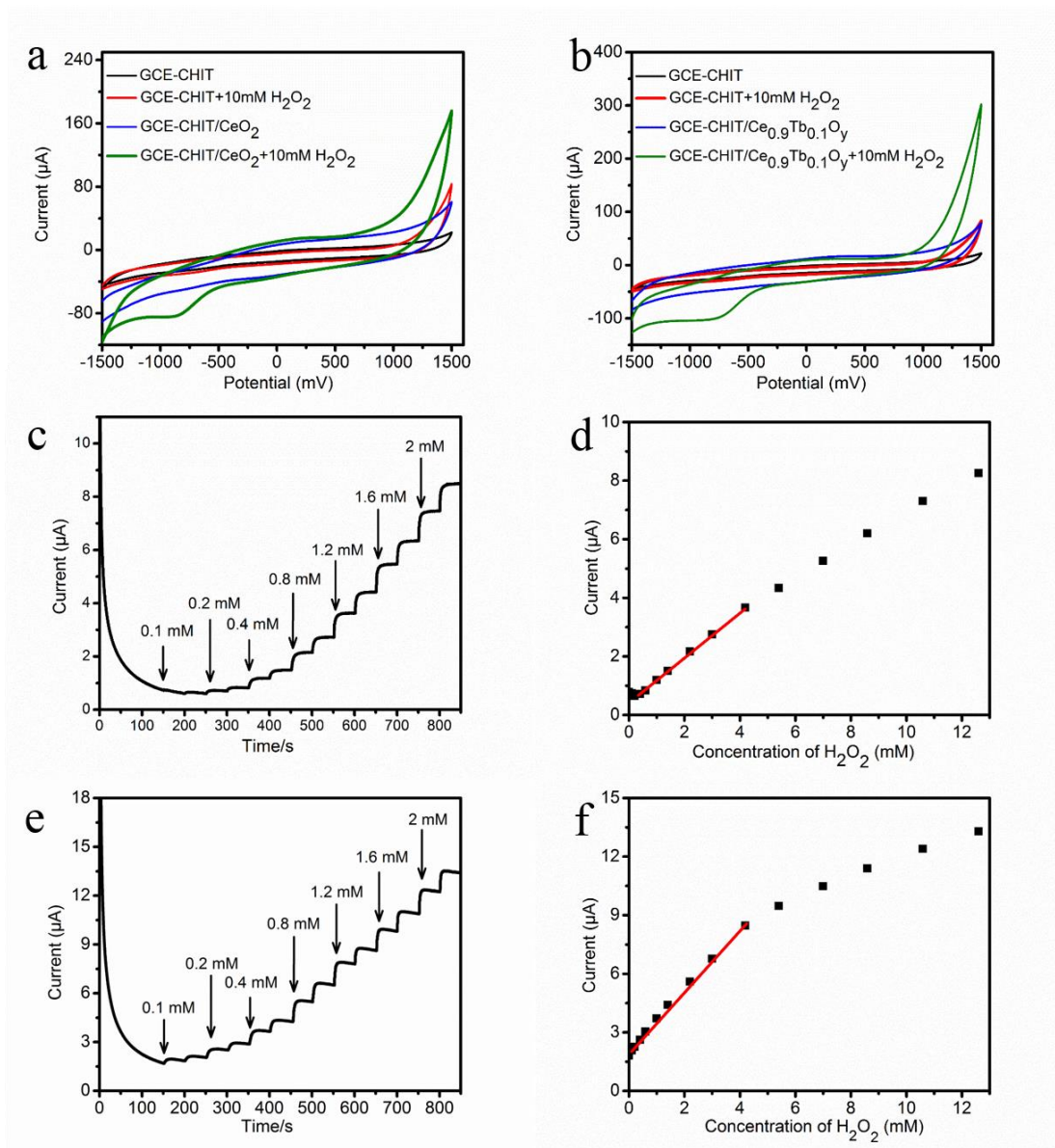


**Fig. 4.** a, Cyclic voltammetry (CV) results of the bear glassy carbon electrode (GCE) GCE-CHIT and GCE-CHIT/CeO<sub>2</sub>; b, GCE-CHIT and GCE-CHIT/Ce<sub>0.9</sub>Tb<sub>0.1</sub>O<sub>y</sub> (b) in the absence and presence of 10 mM H<sub>2</sub>O<sub>2</sub> (Scan rate: 100 mV/s); c and e, Amperometric response of the GCE-CeO<sub>2</sub> and GCE-Ce<sub>0.9</sub>Tb<sub>0.1</sub>O<sub>y</sub> toward different concentrations of H<sub>2</sub>O<sub>2</sub> in 0.1M PBS solution at applied potentials of 0.75 V; d and f, calibration curve for H<sub>2</sub>O<sub>2</sub> using GCE-CeO<sub>2</sub> and GCE-Ce<sub>0.9</sub>Tb<sub>0.1</sub>O<sub>y</sub>.

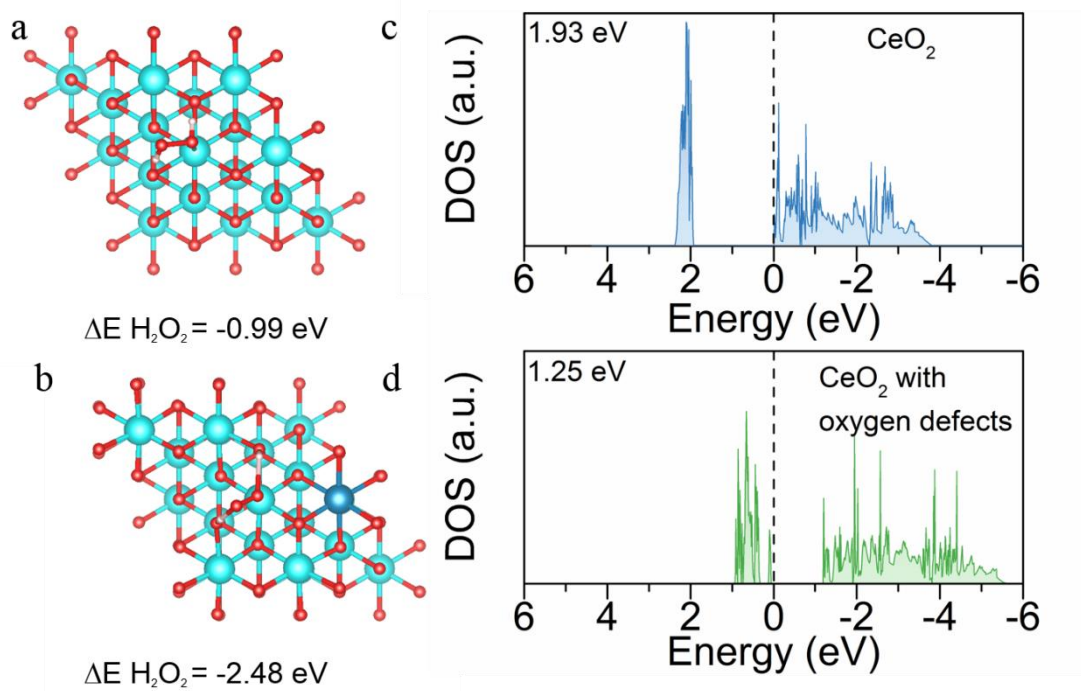


**Fig. 5.** a and b, Adsorption energy of  $\text{H}_2\text{O}_2$  on pure  $\text{CeO}_2$  and  $\text{Ce}_{0.9}\text{Tb}_{0.1}\text{O}_y$  respectively; c and d, the density of state (DOS) of pure  $\text{CeO}_2$  and  $\text{Ce}_{0.9}\text{Tb}_{0.1}\text{O}_y$ , respectively.